

Graphdiyne-Based Ultra-Responsive Artificial Synapse with Multi-Ion Diffusive Dynamics for Mimicking Efferent Nerves

Huanhuan Wei

Nankai University

Rongchao Shi

Nankai University

Lin Sun

Nankai University

Haiyang Yu

Nankai University

Jiangdong Gong

Nankai University

Chao Liu

Nankai University

Zhipeng Xu

Nankai University

Yao Ni

Nankai University

Jialiang Xu

Nankai University

Wentao Xu (✉ wentao@nankai.edu.cn)

Nankai University

Article

Keywords: Graphdiyne, artificial synapse, short-term plasticity, parallel information processing, artificial efferent nerve

Posted Date: August 7th, 2020

DOI: <https://doi.org/10.21203/rs.3.rs-53329/v1>

License:   This work is licensed under a Creative Commons Attribution 4.0 International License.

[Read Full License](#)

Version of Record: A version of this preprint was published at Nature Communications on February 16th, 2021. See the published version at <https://doi.org/10.1038/s41467-021-21319-9>.

Abstract

Somatosensory nerves require synapses to respond efficiently and in parallel for receiving and transmitting biological signals. The gap between biological systems and conventional electronics needs ionotronics to bridge. However, the exploration of new materials and the systematic construction of ionotronics still pose challenges. Graphdiyne, a highly π -extended two-dimensional (2D) carbon allotrope, has demonstrated potential applications in ionic peripheral systems for its inherent network holes that can be used for rapid and selective transmission of diverse ions. Here, a graphdiyne-based artificial synapse (GAS), exhibiting intrinsic short-term plasticity, has been proposed to mimic the biological signal transmission behaviors. A record-breaking impulse responsiveness (± 5 mV) that is an order of magnitude exceeding biological level has been realized for ultra-sensitive and power-efficient brain-inspired applications, with the lowest femtowatt-level consumption (~ 16.7 fW). Most importantly, GAS is capable of parallelly processing signals transmitted from multiple preneurons and therefore realizing dynamic logics and spatiotemporal rules. In a proof-of-concept demonstration, our artificial efferent nerve, connecting GAS with artificial muscles, completes the information integration of preneurons and the information output of motor neurons, which is advantageous for coalescing multiple sensory feedbacks (e.g., visual and tactile) and reacting to these events. Our synaptic element has potential applications in bioinspired peripheral nervous systems of soft electronics and neurorobotics.

Background

Complex human nervous systems, which have the edges of being highly compact, parallel, and reliable, are gaining more and more attention in various fields such as neuromorphic computing, bioinspired sensory systems, and prosthetics.¹⁻⁶ Somatosensory nerves transfer signals through synaptic connections, to achieve a variety of perceptions, memories and motion outputs with different depths.⁷⁻¹⁰ Therefore, the imitation of synapses as building blocks for neural processing are of crucial importance for constructing an efficient artificial neuromorphic system.¹¹⁻¹³ For emulating synaptic behaviors, a variety of structures such as metal/insulator/metal (MIM)-stack switches,¹⁴⁻¹⁸ electrolyte/semiconductor hetero-junctions,^{19,20} and multi-terminal transistors²¹⁻²⁵ have been employed to realize the signal transmission. Among them, the configurations featuring ion migrations can opportunely facilitate the neuromorphic synapses to simulate the biological sensory and motor neurons in bioinspired ionotronic systems. However, the exploration of the working principle of new materials and responsivity of devices are still imperative for achieving biomimetic functionalities.

Highly conjugated π -extended graphdiyne (GDY) has emerged as a new carbon allotrope²⁶⁻²⁸ that serves to enable efficient batteries,²⁹ catalysts,³⁰ solar cells,³¹ nonlinear optics,³² and electronic devices,³³ thanks to their remarkable optical and electric properties.³⁴⁻³⁹ In particular, the engrossing network of GDY with moderate triangular pores and sp -hybridized carbon atoms provides compelling

storage sites and rapid diffusion channels for alkali metal ions and even perchlorate ions.^{35-37,40} Meanwhile, the relatively low diffusion barrier of the ions in GDY contributes to its surface adsorption and interlayer insertion.⁴¹⁻⁴³ These intriguing characteristics inspire a new perspective of constructing GDY-based artificial synapses (GASs) for mimicking synaptic cleft information transmission. Here, for the first time, a junction-type GAS has been proposed by coupling the GDY film with the solid-state electrolytes for emulating multiple short-term plasticity such as postsynaptic current, paired-pulse facilitation (PPF), and dynamic filtering, with an outstanding pulse responsiveness and femtowatt-level energy consumptions. The attempt of utilizing GDY in neuromorphic system has demonstrated the real-time information integration and parallel processing capabilities, and therefore paved the way to future bioinspired ionotronic systems.

Results

General concept. Imitating the principle of biological synaptic cleft, GAS with a junction structure of electrolyte/GDY was fabricated to emulate the essential plasticity (Fig. 1). In biological neurons, the communication between cells hinge on the propagation of action potentials on axons (Fig. 1a). When the action potential reaches the front of the junction, the flow of calcium ions (Ca^{2+}) are triggered and the neurotransmitters are subsequently released, and the sodium ions (Na^+) eventually flow into the postsynaptic membrane (Fig. 1b). Electrolytes with lithium (Li^+) and Na^+ are exploited to prepare GASs, referred to as Li-GAS and Na-GAS, respectively. When a set of positive pulses are applied to the top of the artificial synapse (Fig. 1c), the alkali metal ions (Li^+ and Na^+) are forced to migrate to the gap and accumulate on the surface, or even insert into the interlayer, coinciding the charging process of rechargeable batteries (Fig. 1d).⁴⁰ The investigation of the kinetics of ions at the interface facilitates the modulation of synaptic response. Furthermore, the information integration of parallel processing can be realized using GAS, by connecting with artificial muscles and completing movement responses on artificial efferent neurons.

Fabrication and operation of GAS. Two-dimensional (2D) GDY is produced from the catalytic coupling reaction of its precursor Hexakis[(trimethylsilyl)ethynyl]benzene (HEB-TMS) through the liquid/liquid interfacial protocol (Supplementary Fig. 1a).^{26,27} Atomic force microscope (AFM) image of the as-prepared GDY reveals its 2D nanoflake morphology with a thickness of about 3.3 nm (Fig. 2a). The layered structures with highly wrinkled nanosheets of GDY have been observed under the scanning electron microscope (SEM, Supplementary Fig. 1b). The transmission electron microscope (TEM) images (Fig. 2b and 2c) of the GDY nanoflakes clearly demonstrate their lattice fringes with the lattice spacing of about 0.45 nm, indicating the high crystallinity of the prepared GDY samples.³² The selected area electron diffraction (SAED) patterns further illustrate the good crystallinity of the fabricated GDY (Fig. 2d). The high-resolution X-ray photoelectron spectroscopy (XPS) spectra show the deconvoluted C 1s with major contributions from $\text{C}\equiv\text{C}$ and $\text{C}=\text{C}$ species, indicating the sp - and sp^2 -hybridized carbon atoms of GDY (Fig. 2e). The proportion of sp/sp^2 carbon close to 1.5 is also consistent with the chemical composition of GDY. The presence of sp carbon is also demonstrated by Raman spectrum (Fig. 2f), in

which the characteristic bands at 1932 and 2131 cm^{-1} deriving from the vibration of the conjugated diyne linkage are clearly present.⁴⁴ The flat film of GDY is obtained by spin coating its suspended dispersion in *N,N*-dimethylformamide (DMF) (Supplementary Fig. 1c and 1d), with the thickness of approximately 400 nm (Supplementary Fig. 1e).

To illustrate the dynamics of the migration of anions and cations, the first ten current-voltage (*I-V*) sweeps were performed in Li-GAS and Na-GAS, respectively (Fig. 2g and 2h). An obvious negative differential resistance (NDR) phenomenon has been observed in Li-GAS (Fig. 2g), which is probably due to the migration of Li^+ to the surface and plane of GDY. In this way, the electrochemical doping process occurs. However, two groups of NDRs appear in the *I-V* curve of Na-GAS, of which the NDR at the low potential is more pronounced (Fig. 2h). The very obvious NDR in Na-GAS might be caused by the large internal field formed by the interface ions.⁴⁵ In the positive sweep range, the Li^+ cations are doped in GDY and the anions gradually accumulate at the interface to form an internal field. The intensity of this internal field will temporarily exceed the applied electric field, manifesting an NDR phenomenon and a de-doping process. As the scanning window becomes narrower, the NDR phenomenon disappears, manifesting the effect of interface pseudocapacitance (Supplementary Fig. 2a and 2d). The first eight *I-V* sweeps in Li-GAS were performed to show good reversibility in the low voltage range (Supplementary Fig. 2e and 2f). The response of Na-GAS in the low voltage range is repeatable after the first few sweeps (Supplementary Fig. 2g and 2h). From the analysis of the *I-V* curve, positive and negative pulses with different amplitudes could have an effect on the synaptic weight under the action of interfacial capacitance and electrochemical doping.

Short-term plasticity and ultra-sensitivity of GAS. Synaptic plasticity is modulated by the presynaptic action potentials, which can trigger the Ca^{2+} influx and release the excitatory or inhibitory neurotransmitters to strengthen or weaken the information transmission. The presynaptic pulses with different amplitude, duration, frequency and number are processed by the synaptic device to output different types of current signals, which is a spike-dependent plasticity. In our synaptic devices, Li- and Na- GASs, varying degrees of short-term enhancement have been demonstrated. Under the same presynaptic pulse (+2 V, 440 ms), it is easier for Li^+ ions to be activated and to migrate in the corresponding synaptic device (Fig. 3a). With the gradual increase of the pulse amplitude (from 0.5 to 4 V) in Li-GAS and Na-GAS, the peak value of postsynaptic current increases stepwise from sub-nA to tens of nanoamps, which is a typical spike-voltage dependent plasticity (Fig. 3a).⁴⁶ This plasticity can also be observed under the action of negative pulses (Supplementary Fig. 3a). Under a single pulse stimulus, the surge current decayed to the level of ± 0.2 nA in a short time (< 6 s), showing an obvious bidirectional short-term plasticity of GAS (Supplementary Fig. 3b and 3c). Successive pulse stimulation in a short interval ($\Delta t < 3$ s) will produce paired current peaks of different heights (A1 and A2). As the time interval increases, the PPF effect ($A2/A1 \times 100\%$) becomes weaker (Fig. 3b), which may result from the rapid diffusion of ions provided by the large pores of GDY network. At the same pulse interval, Na-GAS exhibits a higher facilitation index compared to that of Li-GAS. The facilitation index under negative pulses is also relatively lower, which might be attributed to the volatile effect required for short-term plasticity. Negative

pulse sequences with different frequencies have an effect on the peak of postsynaptic current. The higher the pulse rate is, the more obvious the gain ($A_{10}/A_1 \times 100\%$) will be (Fig. 3c), demonstrating a typical spike-rate dependent plasticity (SRDP).⁴⁷ This short-term enhanced plasticity enables GAS to act as a dynamic filter for information transmission.²¹ It is obvious that Li-GAS shows a better dynamic filtering (Fig. 3d), which is consistent with the previous PPF effect (Supplementary Fig. 4a and 4b). As the number and duration of pulses increase, the current gain becomes less pronounced during the charging process and the current decay is still timely during the discharging process (Supplementary Fig. 4c-4f). The reason for this rapid discharge process could be attributed to the ion migration or interface depolarization.¹⁹ Such a rapid volatile process is important for real-time imaging applications through the construction of synaptic array (Fig. 3e). If the letters of "G", "D", and "Y" are input into the array (9×9), the 81-pixel image formed by the array can be refreshed in a short time, thanks to the exemplary short-term plasticity of the synaptic unit. When continuous nonidentical negative pulses are applied, a repeatable short-term plasticity is observed (Fig. 3f). The pulses with different amplitudes correspond well to the different discharge current peaks, which further indicates the good stability and repeatability of GAS, in comparison with solution-processed reduced graphene oxide.⁴⁸ It takes only 0.22 seconds to encode the postsynaptic current triggered by the presynapse of different amplitudes into a pattern with obvious contrasts (Supplementary Fig. 5a and 5b). Such a rapid deintercalation of ions should be attributed to the triangular macroporous structure of the GDY network. Moreover, when 10 and 15 consecutive negative pulses (-3.5 and -5 V) were applied in Li-GAS, the peak current was increased and then quickly declined within a few seconds after removing the pulse (Supplementary Fig. 5c). Such an ion diffusion dynamics also occurs in Na-GAS, resulting in a remarkable pulse sensitivity (Fig. 3g). As the pulse amplitude gradually weakens to the range of 80 to 8 mV, such a plasticity can be still achieved and the average power consumed by a single synaptic event is 16.7 fW, orders of magnitude lower than the biological level and the lowest value so far in the two-terminal devices (Supplementary Fig. 5d). The sensitivity to presynaptic pulses, ultra-low power consumption, and the significant volatility are integral to construct a bioinspired ionic sensory/motor system.

Integration, parallel processing and artificial efferent neuron actuation of GAS. Electrolyte-based devices can convert biologically ionic/chemical signals into electrical signals, and therefore attractive dendritic integration can be possibly realized.¹¹ Multiple input signals applied to the top of GAS will be integrated and output at the bottom (Fig. 4a). Firstly, the rules of spatiotemporal learning of two synapses are simulated. The two synapses exhibit synaptic connections with different strengths under different amplitude pulse stimulation in Li-GAS and Na-GAS (Fig. 4b). When the two synapses act simultaneously, the nonlinear increases of the output prominently. When one of the two synapses are triggered earlier than the other ($\Delta T < 0$) by less than 4 s, the output postsynaptic current will gradually increase to 340% and 250% of the initial output in Li-GAS and Na-GAS (Supplementary Fig. 6a), respectively. Through the input of multiple preneurons, interesting temporal features of dendritic connections have been observed. This also shows that the synergy of multiple synapses (synapse 1 and synapse 2) can significantly enhance the synaptic weight compared to different numbers of repeated stimulation applied to a single synapse (Fig. 4c). In this way, the gain obtained by parallel processing of multiple synapses is much

higher than a single synapse under spike-dependent plasticity. Distributing the weight pressure to a single synaptic unit is the essence of parallel processing. The shared information transmission by multiple synapses resemble better the biological information integration than information transmission by single synapses. Similarly, the gain of the postsynaptic current triggered by presynaptic pulses with different durations in a single synapse is still not as significant as the gain obtained by the integration of multiple synapses (Fig. 4d). Therefore, logic operations can be realized according to the different gains of one synapse and two synapses at different durations (Supplementary Fig. 6b). Meanwhile, the modulation of the neural responses can also be simulated under the synergy of two synapses. Then, shunting inhibition, a mechanism for regulating neural response, can be achieved by applying excitatory and inhibitory pulses to the two synapses respectively (Fig. 4e). With the gradual increase of a presynaptic inhibitory pulse, the postsynaptic current gradually weakens until it disappears. This suggests that the output can be both zoomed in and out during information integration.

The parallel processing of neuromorphic biological signals is of crucial importance in the novel computational paradigm.¹¹ It remains as a challenge for synaptic units to perform real-time parallel processing of external perception information (light and temperature) transmitted by multiple sensory neurons and to make artificial efferent nerves respond differently to the integrated information (Fig. 4f). Here, impulse stimuli of different frequencies are applied to the top electrode of GAS as perceptual information from the outside, and artificial muscles are connected to the bottom electrode of GAS through a circuit to construct artificial efferent neurons (Fig. 4g). Initially, under a single frequency (0.48 Hz) input, the currents generated by two independent synaptic units are close, and their overall outcome is equal to the peak current of the two synapses in the same time period (Fig. 4h). If the two synapses can simultaneously receive signals provided by peripheral devices in the same time period, the signal reflected in the post-neuron is the superposition of the signals obtained by the two independent synapses. The effect of integrating multiple inputs and accumulating outputs is significantly higher than that of a single synapse. Next, the results obtained under different pulse frequency inputs (0.48, 0.8 Hz; 0.344, 0.60 Hz) are consistent, which means the output results of multiple presynaptic pulses in the same time period are accumulated in parallel (Supplementary Fig. 7). Meanwhile, the peak shape of the post-neuronal signal can clearly reflect the time period during which the two synapses receive signals of different frequencies from the peripheral unit, and the frequency of the presynaptic pulse can be inferred from the different peak-to-valley spacing (Supplementary Fig. 7e). Hence, GAS can identify the frequency of presynaptic pulses to a certain extent to infer and analyze the sensory information transmitted from afferent nerves. Finally, as a proof-of-concept, artificial efferent nerves have been constructed to implement the integrated output of multiple synaptic inputs (Supplementary Fig. 8). With only one input terminal, the generated output signal reaches the motor neuron via the efferent nerve to trigger the artificial muscle bending (Fig. 4i). When two sets of inputs are applied, the signals are processed in parallel and output by GAS, and finally transmitted in the efferent nerve to drive the artificial muscle to produce greater bending. Multiple external inputs are integrated in the GAS and the cumulative output drives the artificial muscle. Such a GAS element can process in parallel and integrate the received signals

in real time, and can be combined with a multi-functional actuator to sense or control objects, and can also be coupled with a variety of receivers to sensitively reflect external environmental information.^{1,8,49}

Discussion

Inspired by somatosensory nerves, we have designed and demonstrated the first graphdiyne-based artificial synapse components with the capability of parallel processing and information integration. Benefiting from the special working mechanism of ions migration and good electron transport properties, GAS exhibits essential short-term synaptic behaviors and ultralow voltage response and sub-biological power consumption. As an exceptional parallel processing unit, GAS can identify the frequency of presynaptic inputs to a certain extent based on the postsynaptic current to infer and analyze the sensory information transmitted from afferent nerves. By connecting GAS and artificial motor neurons, artificial efferent nerves are constructed to drive artificial muscles to bend. GAS can process multiple sets of input in parallel and integrate the output to control the degree of bending of artificial muscles. With the implementation of real-time parallel processing, integrating and actuating, the artificial synapse has potential to be a key processing element in a peripheral nervous system of soft electronics, neurorobotics, smart prostheses, and human-machine interactions.

Methods

Fabrication and characterization of multilayer GDY films. HEB-TMS (8 mg) was added to 120 mL of degassed dichloromethane and stirred for 10 min. Then, 100 μ L of tetrabutylammonium fluoride (1 M in THF, 100 μ mol) was injected. The mixture was stirred for another 15 min under an argon atmosphere in the dark. The subsequent reaction can be carried out without purification. The multilayer graphdiyne film was prepared via a liquid/liquid interfacial reaction. Under an argon atmosphere at room temperature, 10 mL of HEB in dichloromethane (0.1 mM) was added to a glass cylinder. Next, 12 mL of deionized water was added to form a layer between the two separate phases. Then, 8 mL of mixture solution consisting of 0.01 M of copper acetate and 0.25 M of pyridine was dropped slowly to the aqueous phase. The system was kept undisturbed for more than 24 h, and a brown film can be observed at the interface. Remove the reagent from the glass cylinder, and the film could be collected and filtered through a nylon membrane with 100-nm pore size and washed by HCl (1 M, 10 mL) and pure water (10 mL). The morphology of the as-prepared GDY was characterized by SEM using a QUANTA FEG 450 field-emission microscope. The crystal features of GDY were characterized by high-resolution TEM (JEM-2800), and the thickness was characterized by AFM (Bruker, Dimension ICON). The Raman spectrum of the GDY was obtained using a high-resolution confocal Raman microscope (TEO, SR-500I-A) at 532 nm excitation. XPS was conducted by a Thermo Scientific ESCALAB 250Xi instrument.

Fabrication of Li-GDY and Na-GDY synaptic devices and electrical measurements. A doped-Si substrate was cleaned by sonication in deionized water, acetone and 2-propanol, boiled in 2-propanol, and then treated with ultraviolet ozone. GDY (5 mg) was placed in DMF (10 mL) and dispersed ultrasonically for 10 min. The resulting GDY dispersion (80 μ L) was spin-coated at 800 rpm on the treated substrate and

annealed at 80 °C for 20 min. Lithium-ion and sodium-ion solid polymer electrolyte (Li-SPE and Na-SPE) were obtained by mixing and stirring PEO powder (0.8 g) with the corresponding perchlorate (0.1 g) in acetonitrile (10 mL). The two electrolytes were spin-coated on the GDY film, and the devices were annealed at 90 °C in a nitrogen-filled glove box for 20 min, after which Au-dot electrodes were deposited subsequently to obtain Li-GAS and Na-GAS. All electrical measurements were characterized using a Keithley 4200A semiconductor parameter analyzer in a nitrogen-filled glove box with moisture and oxygen content of less than 0.1 ppm.

Fabrication of electrolyte layer and actuator. The electrolyte layer was fabricated by dissolving poly(vinylidene fluoride-co-hexafluoropropylene) (PVDF-HFP) and 1-ethyl-3-methylimidazolium tetrafluoroborate (EMIBF₄) in 2 mL of DMF at 60 °C for 1 day to obtain uniform solution. A glass mold was used to prepare the electrolyte layer by solution casting in N₂ atmosphere for 1 day at room temperature, and then, the transparent electrolyte layer was obtained by peeling from the glass. The electrolyte layer was sandwiched by carbon nanotube (CNT) electrodes, which were pressed at 70 °C for 2 min to fabricate the actuator. Subsequently, the as-prepared actuator was aged under a reduced pressure at room temperature for one day, and then cut into strips with the same dimensions (20 × 2 mm²) for further measurements.

Construction of synaptic device- amplifier circuit-polymer actuator system. In order to operate the actuator, we introduce an operational amplifier to output the desired voltage. The bottom electrode of synaptic device was connected to the amplifier circuit to convert currents to output voltages, such that the actuator can be operated. One end of the bottom electrode of synaptic device was coated with silver paste and dried in air. Copper wires were used for connection. The amplifier circuit amplifies the input voltage by 250,000 times to reach the working voltage of the actuator of ~ 3 V.

Data availability

The data that support the plots within this paper and other findings of this study are available from the corresponding author upon reasonable request.

References

1. Kim, Y. *et al.* A bioinspired flexible organic artificial afferent nerve. *Science* **360**, 998-1003 (2018).
2. Zhang, X. *et al.* An artificial spiking afferent nerve based on Mott memristors for neurorobotics. *Nat. Commun.* **11**, 51 (2020).
3. van de Burgt, Y. *et al.* A non-volatile organic electrochemical device as a low-voltage artificial synapse for neuromorphic computing. *Nat. Mater.* **16**, 414-418 (2017).
4. Karbalaee Akbari, M. & Zhuiykov, S. A bioinspired optoelectronically engineered artificial neurorobotics device with sensorimotor functionalities. *Nat. Commun.* **10**, 3873 (2019).

5. Seo, S. *et al.* Artificial optic-neural synapse for colored and color-mixed pattern recognition. *Nat. Commun.* **9**, 5106 (2018).
6. Chen, Y. *et al.* Piezotronic Graphene Artificial Sensory Synapse. *Adv. Funct. Mater.* **29**, 1900959 (2019).
7. Lee, Y. & Lee, T. W. Organic Synapses for Neuromorphic Electronics: From Brain-Inspired Computing to Sensorimotor Nerve Electronics. *Acc. Chem. Res.* **52**, 964-974 (2019).
8. Lee, Y. *et al.* Stretchable organic optoelectronic sensorimotor synapse. *Sci. Adv.* **4**, eaat7387 (2018).
9. Tan, H. *et al.* Tactile sensory coding and learning with bio-inspired optoelectronic spiking afferent nerves. *Nat. Commun.* **11**, 1369 (2020).
10. Choi, D., Song, M.-K., Sung, T., Jang, S. & Kwon, J.-Y. Energy scavenging artificial nervous system for detecting rotational movement. *Nano Energy* **74**, 104912 (2020).
11. van Doremaele, E. R. W., Gkoupidenis, P. & van de Burgt, Y. Towards organic neuromorphic devices for adaptive sensing and novel computing paradigms in bioelectronics. *J. Mater. Chem. C* **7**, 12754-12760 (2019).
12. Wan, C., Xiao, K., Angelin, A., Antonietti, M. & Chen, X. The Rise of Bioinspired Ionotronics. *Adv. Intell. Syst.* **1**, 1900073 (2019).
13. Han, H., Yu, H., Wei, H., Gong, J. & Xu, W. Recent Progress in Three-Terminal Artificial Synapses: From Device to System. *Small* **15**, e1900695 (2019).
14. Yang, J. J., Strukov, D. B. & Stewart, D. R. Memristive devices for computing. *Nat. Nanotechnol.* **8**, 13-24 (2013).
15. Raeis-Hosseini, N., Park, Y. & Lee, J.-S. Flexible Artificial Synaptic Devices Based on Collagen from Fish Protein with Spike-Timing-Dependent Plasticity. *Adv. Funct. Mater.* **28**, 1800553 (2018).
16. Ge, J. *et al.* Memristive synapses with high reproducibility for flexible neuromorphic networks based on biological nanocomposites. *Nanoscale* **12**, 720-730 (2020).
17. Nayak, A. *et al.* Controlling the Synaptic Plasticity of a Cu₂S Gap-Type Atomic Switch. *Adv. Funct. Mater.* **22**, 3606-3613 (2012).
18. Ohno, T. *et al.* Short-term plasticity and long-term potentiation mimicked in single inorganic synapses. *Nat. Mater.* **10**, 591-595 (2011).
19. Dong, W. S. *et al.* Frequency-dependent learning achieved using semiconducting polymer/electrolyte composite cells. *Nanoscale* **7**, 16880-16889 (2015).
20. Liu, G. *et al.* Organic Biomimicking Memristor for Information Storage and Processing Applications. *Adv. Electron. Mater.* **2**, 1500298 (2016).
21. Zhu, L. Q., Wan, C. J., Guo, L. Q., Shi, Y. & Wan, Q. Artificial synapse network on inorganic proton conductor for neuromorphic systems. *Nat. Commun.* **5**, 3158 (2014).
22. Lai, Q. *et al.* Ionic/electronic hybrid materials integrated in a synaptic transistor with signal processing and learning functions. *Adv. Mater.* **22**, 2448-2453 (2010).

23. Shen, A. M. *et al.* Analog neuromorphic module based on carbon nanotube synapses. *ACS Nano* **7**, 6117-6122 (2013).
24. He, Y. *et al.* Spatiotemporal Information Processing Emulated by Multiterminal Neuro-Transistor Networks. *Adv. Mater.* **31**, e1900903 (2019).
25. Gkoupidenis, P., Schaefer, N., Garlan, B. & Malliaras, G. G. Neuromorphic Functions in PEDOT:PSS Organic Electrochemical Transistors. *Adv. Mater.* **27**, 7176-7180 (2015).
26. Li, G. *et al.* Architecture of graphdiyne nanoscale films. *Chem. Commun.* **46**, 3256-3258 (2010).
27. Matsuoka, R. *et al.* Crystalline Graphdiyne Nanosheets Produced at a Gas/Liquid or Liquid/Liquid Interface. *J. Am. Chem. Soc.* **139**, 3145-3152 (2017).
28. Gao, X. *et al.* Direct Synthesis of Graphdiyne Nanowalls on Arbitrary Substrates and Its Application for Photoelectrochemical Water Splitting Cell. *Adv. Mater.* **29**, 1605308 (2017).
29. He, J. *et al.* Hydrogen substituted graphdiyne as carbon-rich flexible electrode for lithium and sodium ion batteries. *Nat. Commun.* **8**, 1172 (2017).
30. Li, J. *et al.* Graphdiyne for crucial gas involved catalytic reactions in energy conversion applications. *Energy Environ. Sci.* **13**, 1326-1346 (2020).
31. Li, J. *et al.* Graphdiyne as a Host Active Material for Perovskite Solar Cell Application. *Nano Lett.* **18**, 6941-6947 (2018).
32. Wu, L. *et al.* Kerr Nonlinearity in 2D Graphdiyne for Passive Photonic Diodes. *Adv. Mater.* **31**, e1807981 (2019).
33. Jin, Z. *et al.* Graphdiyne for multilevel flexible organic resistive random access memory devices. *Mater. Chem. Front.* **1**, 1338-1341 (2017).
34. Huang, C. *et al.* Progress in Research into 2D Graphdiyne-Based Materials. *Chem. Rev.* **118**, 7744-7803 (2018).
35. Gao, X., Liu, H., Wang, D. & Zhang, J. Graphdiyne: synthesis, properties, and applications. *Chem. Soc. Rev.* **48**, 908-936 (2019).
36. Huang, C., Zhao, Y. & Li, Y. Graphdiyne: The Fundamentals and Application of an Emerging Carbon Material. *Adv. Mater.* **31**, 1904885 (2019).
37. Du, Y., Zhou, W., Gao, J., Pan, X. & Li, Y. Fundament and Application of Graphdiyne in Electrochemical Energy. *Acc. Chem. Res.* **53**, 459-469 (2020).
38. Kong, Y. *et al.* Bridging the Gap between Reality and Ideality of Graphdiyne: The Advances of Synthetic Methodology. *Chem*, doi:10.1016/j.chempr.2020.06.011 (2020).
39. Zuo, Z. & Li, Y. Emerging Electrochemical Energy Applications of Graphdiyne. *Joule* **3**, 899-903 (2019).
40. Du, H. *et al.* Graphdiyne applied for lithium-ion capacitors displaying high power and energy densities. *Nano Energy* **22**, 615-622 (2016).
41. Huang, C. *et al.* Graphdiyne for high capacity and long-life lithium storage. *Nano Energy* **11**, 481-489 (2015).

42. Sun, C. & Searles, D. J. Lithium Storage on Graphdiyne Predicted by DFT Calculations. *J. Phys. Chem. C* **116**, 26222-26226 (2012).
43. Farokh Niaei, A. H., Hussain, T., Hankel, M. & Searles, D. J. Sodium-intercalated bulk graphdiyne as an anode material for rechargeable batteries. *J. Power Sources* **343**, 354-363 (2017).
44. Zhou, J. *et al.* Synthesis of Graphdiyne Nanowalls Using Acetylenic Coupling Reaction. *J. Am. Chem. Soc.* **137**, 7596-7599 (2015).
45. Zeng, F., Lu, S., Li, S., Li, X. & Pan, F. Frequency selectivity in pulse responses of Pt/poly(3-hexylthiophene-2,5-diyl)/polyethylene oxide +Li⁺/Pt hetero-junction. *PLoS One* **9**, e108316 (2014).
46. Kim, S. I. *et al.* Dimensionality Dependent Plasticity in Halide Perovskite Artificial Synapses for Neuromorphic Computing. *Adv. Electron. Mater.* **5**, 1900008 (2019).
47. Zhang, S.-R. *et al.* Artificial Synapse Emulated by Charge Trapping-Based Resistive Switching Device. *Adv. Mater. Technol.* **4**, 1800342 (2019).
48. Park, M.-J., Park, Y. & Lee, J.-S. Solution-Processed Multiterminal Artificial Synapses Based on Ion-Doped Solid Electrolytes. *ACS Appl. Electron. Mater.* **2**, 339-345 (2020).
49. Wan, C. *et al.* An Artificial Sensory Neuron with Tactile Perceptual Learning. *Adv. Mater.* **30**, e1801291 (2018).

Declarations

Acknowledgements

This research is supported by Tianjin Science Foundation for Distinguished Young Scholars (19JCJQC61000), National Natural Science Foundation of China (21773168), Key Area R&D Program of Guangdong Province (2018B030338001), Hundred Young Academic Leaders Program of Nankai University (2122018218), Natural Science Foundation of Tianjin (18JCYBJC16000), the 111 Project (B16027 and B18030), the International Cooperation Base (2016D01025), and Tianjin International Joint Research and Development Center.

Author contributions

H.W., R.S., and L.S. contributed equally to this work. W.X., J.X. and H.W. conceived the original concept and designed the experiments. R.S. and C.L. synthesized and characterized the GDY. H.W. fabricated the devices and performed electrical measurements. W.X. and L.S. designed the systems and prepared the circuits. H.W., R.S. and L.S. wrote the manuscript with input from all the other authors. All authors discussed the results and commented on the manuscript.

Competing interests

The authors declare no competing interests.

Additional information

Figures

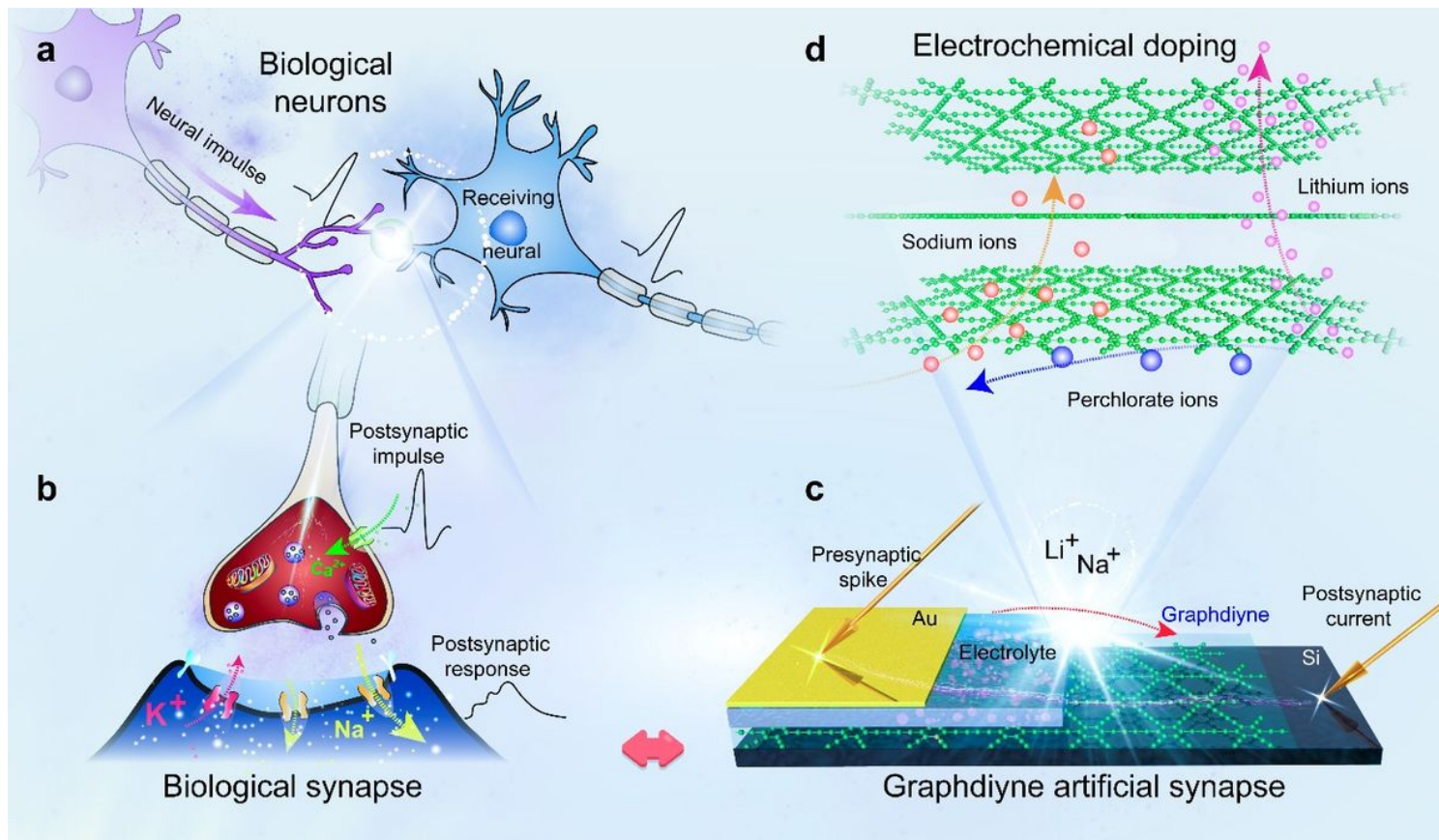


Figure 1

Schematic illustrations of the graphdiyne-based artificial synapse (GAS) with multi-ion diffusive dynamics. a The signal transmission between neurons. b The ion flows in the synaptic cleft. c The junction-type GAS. d The dynamic diffusion process of ions between GDY layers.

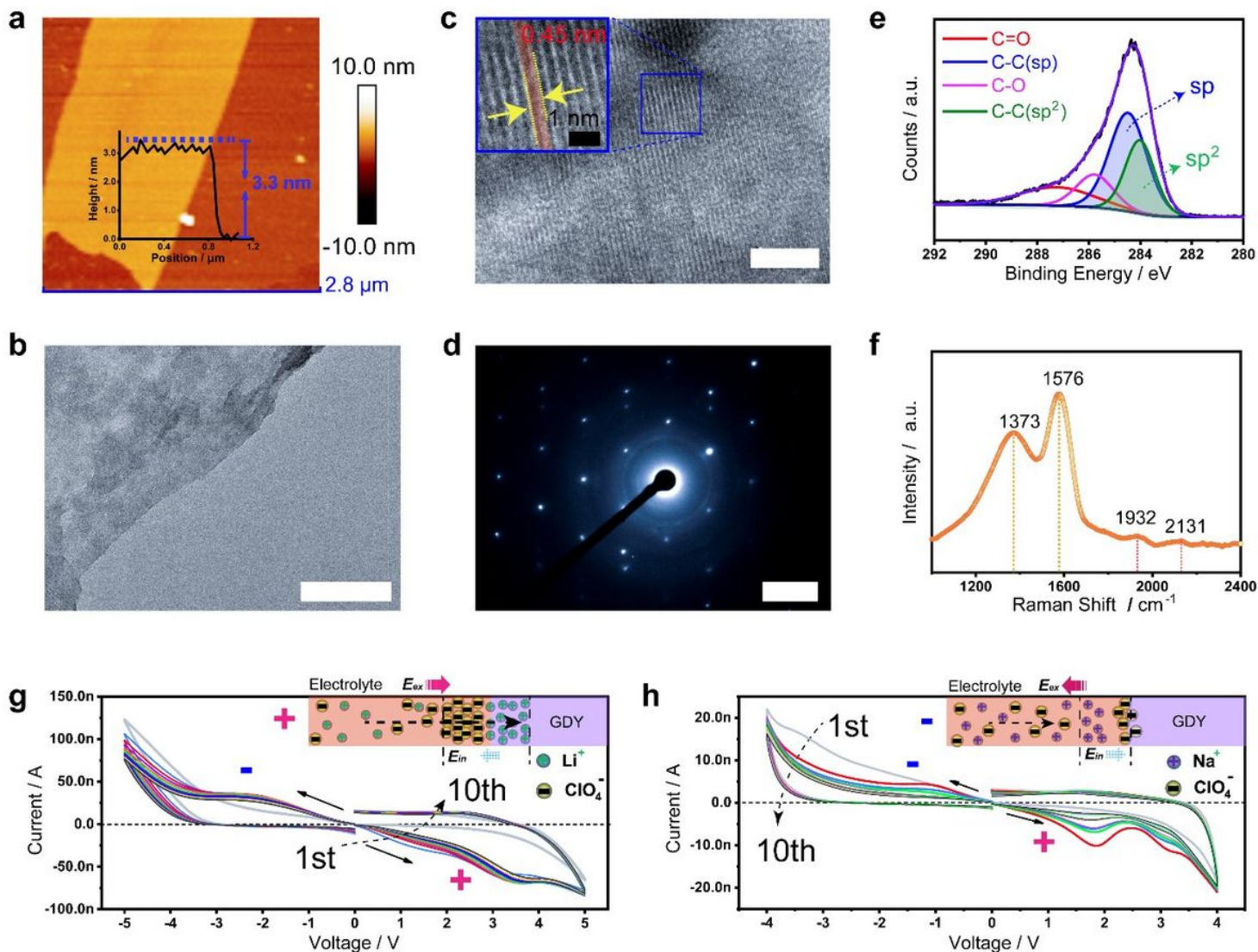


Figure 2

Characterizations of GDY and GASs. a AFM image, b TEM image (Scale bar: 200 nm), c high-resolution TEM image (Scale bar: 5 nm), d SAED pattern (Scale bar: 5 1/nm), e high-resolution XPS spectra of C 1s, and f Raman spectrum of GDY. g, h I-V curves measured in sweep cycles of 0 to 5 V and 0 to -5 V in Li-GAS and Na-GAS, respectively. Inset: Schematic illustrations of ion dynamic diffusions under positive and negative pulses.

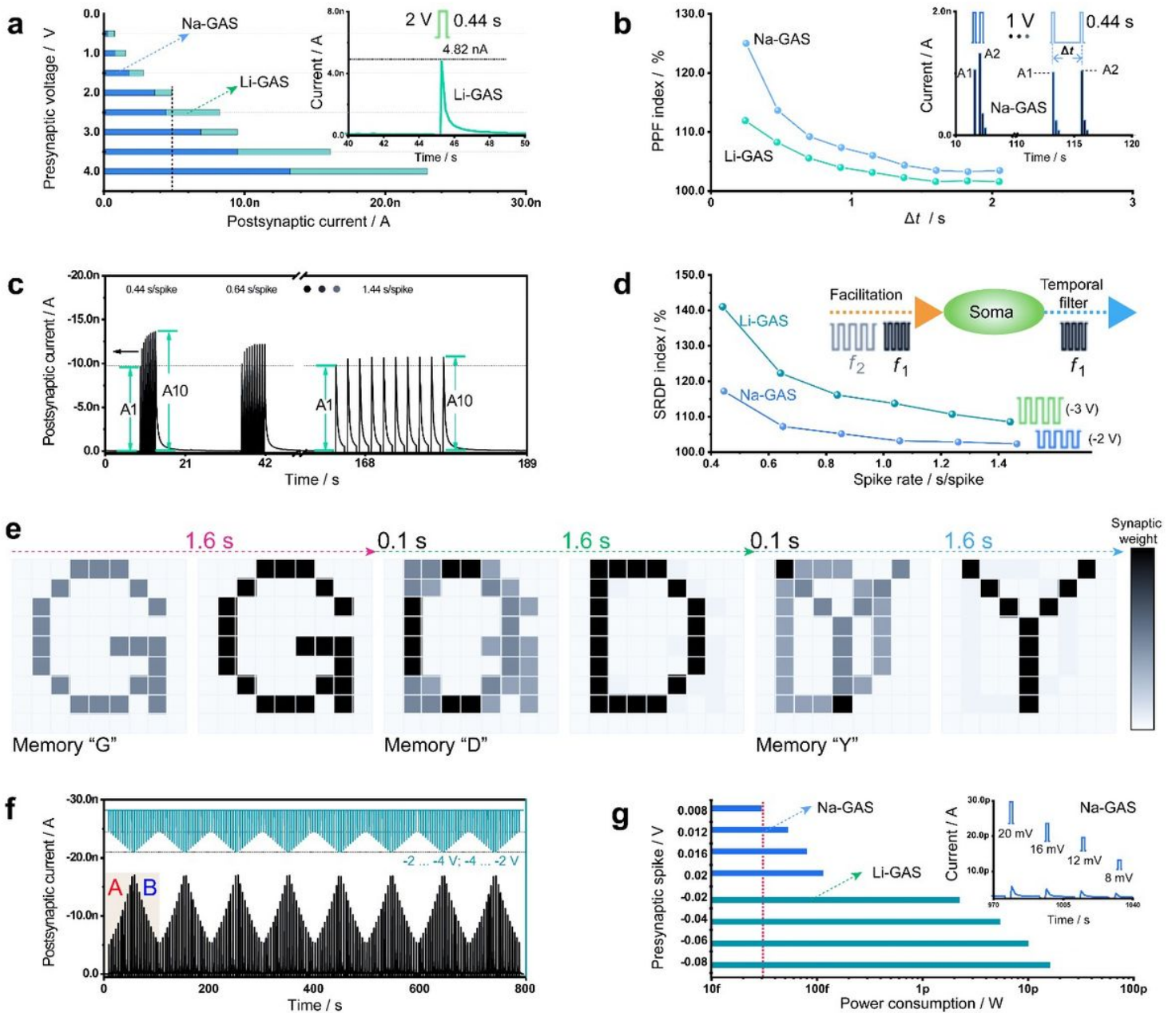


Figure 3

Short-term plasticity in Li- and Na- GASs. a Peak value of postsynaptic current with different positive pulse amplitudes in Li-GAS and Na-GAS, respectively. Inset: Postsynaptic current triggered by a single spike in Li-GAS. b PPF behavior emulated by two consecutively positive pulses (+1 V) in Li-GAS and Na-GAS, respectively. Inset: Postsynaptic currents triggered by two spikes in Na-GAS. c Postsynaptic current at different frequencies in Li-GAS. d Gain of postsynaptic currents (SRDP index; $A_{10}/A_1 \times 100\%$) plotted as a function of presynaptic spike rate in Li-GAS and Na-GAS. e Real-time storage and transformation of letters "G", "D", and "Y". f Postsynaptic current triggered by nonidentical negative pulse sequence in Li-GAS. g Impulse responsivity at millivolt level and corresponding power consumption in Li-GAS and Na-GAS. Inset: Postsynaptic currents triggered by a series of positive presynaptic spike voltage amplitude from 8 to 20 mV.

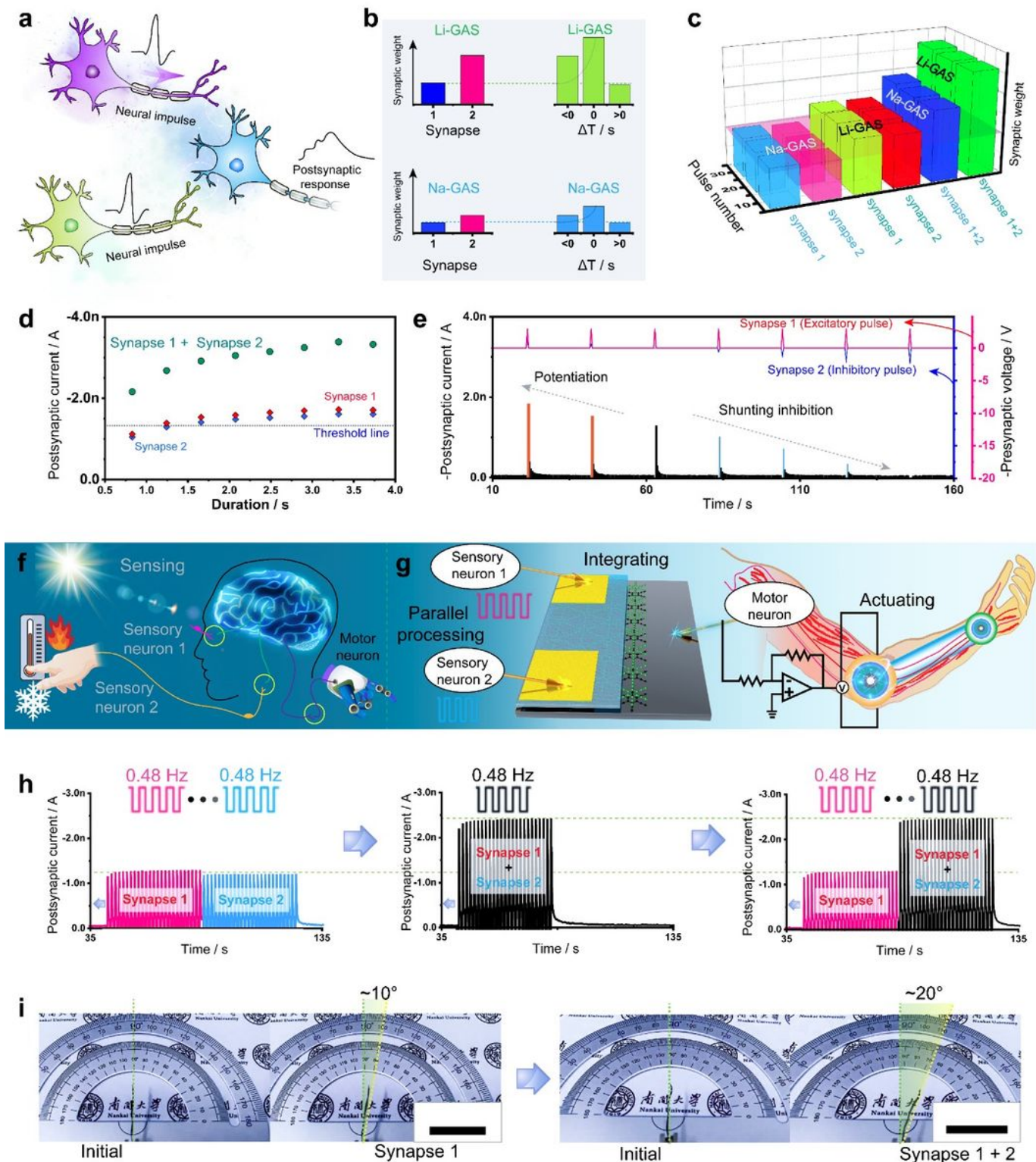


Figure 4

Dendritic integration function in Li- and Na- GASs. **a** Schematic illustration of spatiotemporal neural networks in GAS. **b** Synaptic weight (current) triggered by a single pulse and a pair of spatiotemporally correlated pulses respectively in Li-GAS and Na-GAS. **c** Synaptic weight (current peak value) obtained under different number of applied pulses ($N = 10, 20, \text{ and } 30$) in Li-GAS and Na-GAS. **d** Postsynaptic current obtained under different duration of applied spikes in Li-GAS. **e** Postsynaptic currents triggered by

a pair of presynaptic (excitatory and inhibitory) pulses for emulating shunting inhibition function. Schematic illustration of f biological sensorymotor nervous and g artificial efferent nerve, coupling GAS processing element with artificial muscles, to transduce signals from receptors to motor neurons. h Postsynaptic current triggered by two presynaptic inputs at 0.48 Hz from the same time period to different time periods. i Digital images of the actuator flexion under 0.8 Hz pulse sequences in single and double synapses. The scale bar corresponds to 2 cm.

Supplementary Files

This is a list of supplementary files associated with this preprint. Click to download.

- [FigureS1.jpg](#)
- [FigureS2.jpg](#)
- [FigureS3.jpg](#)
- [FigureS4.jpg](#)
- [FigureS5.jpg](#)
- [FigureS6.jpg](#)
- [FigureS7.jpg](#)
- [FigureS8.jpg](#)